J. Appl. Comput. Mech., xx(x) (2026) 1-13
DOI: 10.22055/jacm.2026.48727.5456

ISSN: 2383-4536
jacm.scu.ac.ir

Shahid Chamran University of Ahvaz

Journal of Applied and Computational Mechanics

Research Paper

Modeling of the Ammonia Substitution Ratio in a Heptane-Fueled Internal Combustion Engine

Samuel Molima[1,2], Fathi Hamdi[1], Takwa Hamdi[1], Mouldi Chrigui[1]

[1] Laboratory for Mechanical Modeling, Energy and Materials (LM2EM), Engineering National School of Gabes, The University of Gabes, Omar Ibn El Khattab Street 6029, Gabes, Tunisia, Email: samuel.molima@enig.rnu.tn (S.M.) fathi.hamdi@enig.u-gabes.tn (F.H.); hamdiitakwaa@gmail.com (T.H.); Mouldi.Chrigui@enig.rnu.tn (M.C.)

[2] Laboratoire de Modélisation Mécanique, Energétique et Matériaux, Institut supérieur des Techniques Appliquées (ISTA-Kinshasa), Avenue Aérodrome N° 3930, Commune de Barumbu, Kinshasa BP 6593, Democratic Republic of the Congo

Received September 01 2025; Revised March 31 2026; Accepted for publication April 14 2026.
✉ Corresponding author: S. Molima (samuel.molima@enig.rnu.tn)

Abstract. Ammonia is a carbon-free, low-emission fuel with high potential for sustainable RCCI engines. This study investigates ammonia–heptane dual-fuel combustion using a hybrid G-equation with detailed chemical kinetics and CFD-based turbulence–chemistry modeling. Increasing ammonia substitution ratio (ASR) reduces peak in-cylinder pressure (up to ~10% at 40% ASR) and heat release rate due to its low reactivity and high ignition energy, while increasing droplet size, vapor penetration, and wall-film formation. At 40% ASR, start-of-injection (SOI) strongly affects emissions: retarded injection (14–16° BTDC) minimizes NO_x (1.73 g/kWh, ~15% lower than 18° BTDC) and CO (1.47 g/kWh, ~70% lower than advanced SOI) but slightly increases unburned hydrocarbons (1.73 g/kWh, ~20% higher), whereas advanced injection (22–24° BTDC) improves UHC conversion but sharply increases CO (~5 g/kWh, +240%) and NOx (3.23 g/kWh, +85%). Pareto-based analysis identifies 16–18° BTDC as the optimal SOI window, balancing fuel efficiency and emissions. These findings provide quantitative guidance for low-carbon RCCI engine optimization.

Keywords: Ammonia/heptane, IC engine, CFD, Low-carbon-fuels, Detailed reaction mechanism, Spray.

1. Introduction

The urgency to reduce reliance on fossil fuels has become more pressing than ever due to stringent environmental regulations and the global drive toward carbon neutrality. This shift has intensified interest in alternative fuels, with ammonia emerging as a promising candidate to address sustainability challenges in transportation and energy sectors [1-3].

Ammonia's use as an engine fuel dates back to World War II, when fuel shortages prompted experimental applications in buses [4-6]. It was first utilized in internal combustion engines (ICEs) as early as 1943. With advancements in engine technology, the relevance of ammonia as a clean fuel has re-emerged. Numerous studies highlight its potential as a viable substitute for conventional fossil fuels, either as a standalone fuel or as part of a dual-fuel system [7, 8].

Ammonia's adoption has been particularly prominent in maritime applications, where the high compression ratios of marine engines align with its physical and chemical properties and enable auto ignition under appropriate conditions. Nevertheless, challenges arise from ammonia's Lower Heating Value (LHV), high autoignition temperature, relatively slow chemical reactivity, and narrow flammability limits, which often necessitate a secondary pilot fuel with a lower autoignition temperature to ensure reliable ignition [9-11]. Despite these challenges, ammonia continues to show strong potential for enhancing thermal efficiency and reducing harmful emissions in dual-fuel compression ignition engines when paired with advanced combustion strategies [12, 13].

Recent experimental studies have demonstrated ammonia's potential in dual-fuel high-pressure direct injection (HPDI) engines. Nadimi et al. [14], reported substantial CO_2, CO, and PM reduction with ammonia-diesel substitution up to 84.2%, albeit with unburned ammonia. Xu et al. [15], showed that advancing ammonia injection in a tri-fuel blend (diesel, ammonia, and methane) reduced CO by 89%. Shin and park [16] demonstrated that direct ammonia injection with a 50% energy ratio reduced NO_2 by 13.5% and GHG emissions by 91%. Collectively, these studies confirm the importance of precise injection strategies and pilot fuel management for efficient low-carbon operation.

Yousefi et al. [17], demonstrated that advancing NH_3 injection timing increased the ammonia energy fraction in an ammonia-diesel dual-fuel (ADDF) configuration, resulting in a 58.8% reduction in NO_x emissions. Earlier work by Reiter and Kong [12] explored 40-60% ammonia blends, finding reduced CO and HC emissions alongside variable NO_x levels and unburned ammonia concentrations of 1000-3000 ppm. Similarly, Bjorgen, et al. [18] investigated diesel mixed with liquid ammonia at ratios of 40%, 50%, and 60%, identifying opposing trends in NO_x and N_2O under conditions of peak combustion efficiency. Elkelawy et al. [19], tested ammonia hydroxide-diesel blends with gaseous enrichment, varying ammonia content from 7.5% to 92.5%, and reported thermal efficiency improvements of 21-24%. Tutak et al. [20], assessed ammonia additions up to 23% in diesel engines, observing increased efficiency and higher peak heat release rates.

Published online: April 16 2026

Qian et al. [21] used NH_3-n-dodecane blends with ammonia proportions ranging from 75.5% to 91.4%, which lead to lower THC and CO emissions. Cheng et al. [22], evaluated n-heptane blended with ammonia 80-98% ammonia energy fraction), revealing that increasing the ammonia content led to extended ignition delays and earlier CA50. Lastly, Mi et al. [23], examined ammonia-diesel blends with energy fractions of 40%, 50%, 60%, and 70%. Their results showed that implementing a pilot injection strategy reduced unburned ammonia by 13% and improved indicated thermal efficiency (ITE) by 45%. High-fidelity computational studies have increasingly leveraged LES-based CFD to resolve detailed spray–combustion interactions. Shi et al. [21] used advanced modeling to explore pilot-assisted ammonia-diesel combustion, highlighting extended ignition delays, improved indicated thermal efficiency, and reduced unburned ammonia with stratified injection.

These studies collectively confirm ammonia's potential to decarbonize ICEs, but they also expose persistent gaps. Existing work often relies in simplified kinetics, idealized combustion chambers, or limited parametric sweeps, leaving the interplay between ASR, spray behavior, and combustion dynamics insufficiently resolved. Moreover, most studies neglect advanced spray-combustion coupling, limiting predictive fidelity.

The objective of the present study is to advance understanding of ammonia-heptane dual-fuel RCCI combustion by examining how varying ASRs influence spray behavior, combustion phasing, emissions, and thermal fields using a high-fidelity, RANS-based CFD framework. The simulations employ detailed chemical kinetics and advanced turbulence and spray models, enabling systematic insights into ammonia-heptane interactions. Special emphasis is based on the emissions pathway analysis, clarifying how ammonia reactivity governs in-cylinder combustion dynamics.

The main contributions are as follows:

1) adoption of a detailed chemical mechanism comprising 74 species and 495 reactions, enabling accurate modeling of ammonia's ignition chemistry and pollutant formation, in contrast to simplified mechanisms often used previously;
2) integration of a hybrid G-equation combustion model with KH-RT spray breakup and wall-film modeling a coupling rarely applied in ammonia-fueled RCCI simulations;
3) a comparative mesh and timestep sensitivity analysis to achieve accuracy within a computationally efficient RANS framework an often-overlooked aspect in similar studies;
4) a thorough investigation of spray characteristics and wall-film dynamics across different ASRs, offering new insights into droplet evolution, vapor penetration, and surface interaction;
5) extensive validation against experiments, simultaneously matching in-cylinder pressure, heat release rate (HRR), and emissions (NO, CO, HC),
6) detailed visualization of temperature and velocity fields to elucidate ignition-zone behavior, flame development, and turbulence-chemistry interaction;
7) employment of a realistic 60° sector geometry with diesel (heptane) pilot injection and premixed air-ammonia, providing a more faithful representation of engine operation than constant volume or single-zone models.

This study combines ASR and SOI sweeps with a hybrid G-equation, detailed chemical kinetics, and advanced spray models (KH-RT and droplet collisions) to achieve high-fidelity ammonia-heptane RCCI combustions, including Pareto-based optimization of SOI for the best trade-off between fuel efficiency and emissions.

The paper is organized as follows: Section 1 reviews relevant prior studies and establishes the state of the art. Section 2 describes the numerical methodology. Section 3 presents the computational setup and boundary conditions. Section 4 reports and discusses the results, and Section 5 concludes the work.

2. Numerical Method

2.1. Governing equations and models for the two-phase flow

The liquid-gas interactions are described using the Eulerian-Lagrangian framework, in which the gas phase is treated as a continuous medium (Eulerian description), while the dispersed liquid droplets are tracked in a Lagrangian manner. This hybrid approach enables accurate modeling of spray breakup, vaporization, transport, and coupling with the surrounding gas, which are critical for RCCI combustion.

2.1.1. *Transport equations for description of the continuous phase*

The gas-phase flow is governed by the Favre-averaged conservation equation of mass, momentum, and stress, whose formulations are standard [24]. These equation account for compressibility, turbulence and source terms associated with spray evaporation and momentum exchange. The energy equation, which is central to combustion and spray-gas thermal coupling, is expressed:

$$\frac{\partial \bar{\rho}\tilde{I}}{\partial t} + \nabla.\left(\bar{\rho}\tilde{u}\tilde{I}\right) = -\bar{p}\ \nabla.\tilde{u} - \nabla.\bar{J} - \nabla.\mathrm{H} + \bar{\rho}\Phi + \dot{\tilde{Q}}^{C} + \dot{\tilde{Q}}^{S} \tag{1}$$

Total flux heat:

$$\bar{J} = -\lambda\nabla\bar{T} - \bar{\rho}D\sum_{k}\tilde{h}_{k}\nabla\bar{y}_{k'} \tag{2}$$

The notation (bar) stands for the Reynolds and (tilde) for Favre-averaging. The quantity $\dot{\bar{\rho}}^{s}$ is the averaged source term related to spray evaporation, $\tilde{u}$ the Favre averaged velocity, while ρ represents the fluid density. The variable $\bar{\sigma}$ denotes the average viscous shear tensor, $\bar{F}^{s}$ the source term due to spray injection, p represents the pressure, and Γ the Reynolds stress tensor. $\bar{J}$ is the total heat flux including the enthalpy diffusion and heat conduction with λ as thermal conductivity. The parameters $\nabla\bar{T}$ expresses the gradient of temperature field in the fluid, D the diffusion coefficient of species, $\tilde{h}_{k}$ the specific enthalpy of species and $\nabla\bar{y}_{k'}$ the gradient of the concentration of species k'. The quantities $\dot{\tilde{Q}}^{C}$ and $\dot{\tilde{Q}}^{S}$ are source terms due to heat release and spray, respectively. Note that H is the heat flux and $\tilde{\varepsilon}$ the dissipation rate of turbulent kinetic energy. The quantity ν in Eq. (3) expresses the kinematic fluid viscosity. The effective species diffusivity and thermal conductivity are modeled as:

$$D_{eff} = D + \frac{\nu_{t}}{S_{C_{t}}} \tag{3}$$

$$k_{eff} = k + \frac{c_{p}\mu_{t}}{P_{r_{t}}} \tag{4a}$$

with,

$$S_{C_t} = 0.7,\ P_{r_t} = 0.9 \tag{4b}$$

where D is the molecular diffusivity, k the thermal conductivity, ν_t the turbulent kinematic viscosity, μ_t the turbulent dynamic viscosity, S_{C_t}.is the turbulent Schmidt number and P_{r_t} is the turbulent Prandtl number

2.2. RNG $k-\varepsilon$ turbulence model

The k-ε model is employed [1, 25, 26], which improves predictions in high-shear and swirling flows. It accounts for non-linear eddy interactions, scale-dependent mean-strain effects, and spray-generated gradients relevant to engine sprays [27, 28]. The standard RNG $k-\varepsilon$ formulation is used as described in literature [29, 30]. With respect to the standard model, the coefficient $C_{\varepsilon 3}$ is adjusted within the range of -0.9 to 1.726 to better represent compressibility effects and rapid distortion in engine-like swirling flows, following the approach of Han and Reitz [27]. The remaining model constants ($C_{\varepsilon 1}$ = 1.42, $C_{\varepsilon 2}$ = 1.68, $C_{\varepsilon 1}$ = 1.5, $1/P_{r_k}$ = $1/P_{r_k}$ = 1.39) retain their standards RNG values.

2.3. Description of the dispersed phase and spray model

Since the Lagrangian approach is used to track the dispersed phase, the governing equations are:

(1) Droplet motion equation: Assumes that discrete evaporating droplets are affected only by inertia, aerodynamic drag, and gravity. The net force balance relates the particle inertia to acting forces.

(2) Droplet temperature equation: Governs droplet evaporation, modeled using the DMC model [31].

Addition, the spray breakup process is modeled via a hybrid KH/RT mechanism [32].

- The KH process governs initial breakup of the liquid spray.
- The RT process governs secondary break-up events [33].

2.4. Species transport model and combustion

In the combustion chamber, the gas phase is modeled as individual gas species. During combustion in a Compression Ignition (CI) Engine, this composition evolves to molecular diffusion, convection, turbulent transport, and chemistry-turbulence interaction. The governing equation for $\bar{Y}_m$ is expressed as:

$$\frac{\partial \bar{\rho}\bar{Y}_m}{\partial t} + \nabla.(\bar{\rho}\bar{u}\bar{Y}_m) = \nabla.(\bar{\rho}D\nabla\bar{Y}_m) + \nabla.(\ \overline{u_m''Y_m''}) - \bar{\rho}\dot{\omega}_m + \dot{\bar{\rho}}_m^C + \dot{\bar{\rho}}_m^S \tag{5}$$

where ρ, and $\bar{u}$ are the density and flow velocity vector, respectively. The subscript m is the species index, D denotes the mixture-average molecules diffusions, $\bar{Y}_m = \bar{\rho}_m/\bar{\rho}$ is the mass fraction of species m, $\dot{\bar{\rho}}_m^S$ is the source term due to spray vaporization, and $\dot{\bar{\rho}}_m^C$ is the source term due to chemical reactions. The chemical source term $\dot{\bar{\rho}}_m^C$ is expressed as:

$$\dot{\bar{\rho}}_m^C = W_m \sum_{i=1}^{I} \dot{\omega}_{mi} \tag{6}$$

where W_m is the molecular weight of species m, and $\dot{\omega}_{mi}$ is the production/dissipation rate of species m in reaction i. This production rate is modeled following as [34]:

$$\dot{\omega}_{mi} = (v_{mi}'' - v_{mi}')q_i \tag{7}$$

The term q_i represents the rate of progress of specified reaction i, while $v''$and v' are the stoichiometric coefficients for products and reactants, respectively.

In the turbulence model, the gradient assumption is used for the turbulent transport of the scalar quantities [35, 36]:

$$\rho u_j'' \Phi'' = -\Gamma_{\Phi,T}\ \nabla\tilde{\Phi}_g \tag{8}$$

where $\Gamma_{\Phi,T}$ denotes the turbulent exchange coefficient for a scalar quantity Φ. For mass transfer, $\Gamma_{Ym,T} = \bar{\rho}D_T$ with the turbulent diffusion coefficient D_T = $\mu_T/(\bar{\rho}S_{C,T})$, where $Sc_{,T}$ is the turbulent Schmidt number, and for energy transfer, $\Gamma_{T,T} = K_T/cp$ with the turbulent thermal conductivity K_T is modeled by $K_T = \mu_T cp/Pr_T$ where Pr_T denoting the turbulent Prandtl number. The combustion modeling leverages a hybrid strategy:

- The flame propagation model to track premixed fronts [36, 37].
- Coupling with a scalar transport equation that captures turbulent flame stretch effects.
- Detailed chemical kinetics resolve local species interactions, while turbulence-chemistry interaction accounts for flame wrinkling and non-premixed burning modes.

2.5. G-equation model

The species transport by solving a scalar field equation, thereby reducing computational cost. A hybrid combustion framework is employed in which detailed finite-rate chemistry governs auto-ignition and diffusive combustion, while the G-equation is activated after ignition and initialized from the chemistry-resolved reaction zone to track premixed NH_3–air flame propagation consistently with local thermochemical states. The G-field is initialized from an iso-surface of temperature as the progress indicator, corresponding to the nascent reaction zone resolved by finite-rate chemistry; specifically, the iso-surface T = 1100 K is used to define the initial flame front position, ensuring consistency with the local species composition and thermal state predicted by detailed kinetics. The G-equation is activated when the local temperature exceeds 1100 K and the volumetric heat-release rate is positive ($\dot{q}$ > 0 J/m^3·s), indicating the formation of a self-sustained reaction zone and the transition from kinetically controlled auto-ignition to propagating premixed combustion; prior to this transition the G-equation is inactive. The effect of the G-field is introduced into the species transport equation (Eq. (10)) through a reaction-rate source term: in cells where G ≤ 0 (burned side), the finite-rate chemistry source term is replaced by the G-equation flamelet contribution, computed as the product of the unburned mixture density, the turbulent flame speed S_T^O (evaluated from Eq. (11), and the magnitude of the G-field gradient $|\nabla\vec{G}|$. In cells where G > 0 (unburned side), the standard finite-rate chemistry source term is retained. This coupling ensures a smooth and physically consistent transition between the auto-ignition and flame-propagation regimes. Variation of $\pm$5% in threshold values did not significantly affect ignition phasing or peak pressure ($<$ 1.5% variation).

The model distinguishes two combustion regimes [38, 39]:

1. Corrugated Flamelet Regime: entirely reactive-diffusive flame structure embedded within Kolmogorov-scale eddies.
2. Thin Reaction Zone Regime: Kolmogorov eddies penetrate the preheat zone of the flame but not the inner reaction layer.

The Favre-averaged transport for the flame front $(\tilde{G})$ and its variance $(\widetilde{G''^2})$ are:

$$\frac{\partial \tilde{G}}{\partial t} + (\tilde{u} - \tilde{u}_{vertex})\nabla \tilde{G} = \frac{\bar{\rho}_u}{\bar{\rho}_b} S_T^O \left|\nabla \tilde{G}\right| - D_T \tilde{k} \left|\nabla \tilde{G}\right| \tag{9}$$

$$\frac{\partial \widetilde{G''^2}}{\partial t} + \tilde{u}\nabla \widetilde{G''^2} = \nabla_{\|} \cdot \left(\frac{\mu_t}{\bar{\rho}_b} D_T \nabla_{\|} \widetilde{G''^2} \right) + 2 D_T (\nabla \tilde{G})^2 - C_S \frac{\tilde{\varepsilon}}{\tilde{k}} \widetilde{G''^2} \tag{10}$$

where $\tilde{G}$ and $\widetilde{G''^2}$ are the (Favre-averaged) field equation of instantaneous flame position and its variance, respectively. $\nabla_{\|}$ is the tangential gradient operator, $\tilde{u}$ the averaged vector of velocity, and $\tilde{u}_{vertex}$ the velocity of the moving vertex. The quantities $\bar{\rho}_u$ and $\bar{\rho}_b$ are the densities of the fresh and burned mixture, respectively. D_T is the turbulent diffusivity, C_S is a model constant, $\tilde{k}$, and $\tilde{\varepsilon}$ are the Favre mean turbulent kinetic energy and its dissipation rate, respectively, as already mentioned. The turbulent flame speed, S_T^O used in Eq. (11) is modeled as [40-43]:

$$\frac{S_T^O}{S_L^O} = 1 + I_P \left\{ -\frac{a_4 b_3^2}{2 b_1} \frac{l_I}{l_F} + \left[\left(\frac{a_4 b_3^2}{2 b_1} \frac{l_I}{l_F} \right)^2 + a_4 b_3^2 \frac{u'}{S_L^O} \frac{l_I}{l_F} \right]^{1/2} \right\}, \tag{11}$$

where I_P represents a progress variable, which models physically the increasingly disturbing effect of the surrounding eddies on the flame front surface as the spark ignition kernel flame grows from the laminar stage into the fully developed turbulent stage [40], S_L^O is the laminar flame speed, l_I the turbulence Integral length scale, l_F the laminar flame thickness, and u' the turbulence intensity. a_4, b_1 and b_3 are model constants.

To capture detailed chemical kinetics, a reaction mechanism for n-heptane–ammonia blends, validated by Wang et al. [44], is employed. The mechanism includes 74 species and 495 reactions and fully resolves nitrogen oxide pathways, including N_2O, NO, and NO_2, providing a robust framework for accurately predicting both combustion and emissions.

The pre-tabulated quantities, such as laminar flame speed, species concentrations, and heat release rates, are applied as source terms at the flame front, ensuring a physically consistent and computationally efficient representation of combustion. This approach allows the simulation to capture essential flame dynamics, species evolution, and NO_x formation in turbulent premixed and partially premixed conditions, while maintaining high fidelity and significantly reducing computational cost compared to solving the full mechanism in real time.

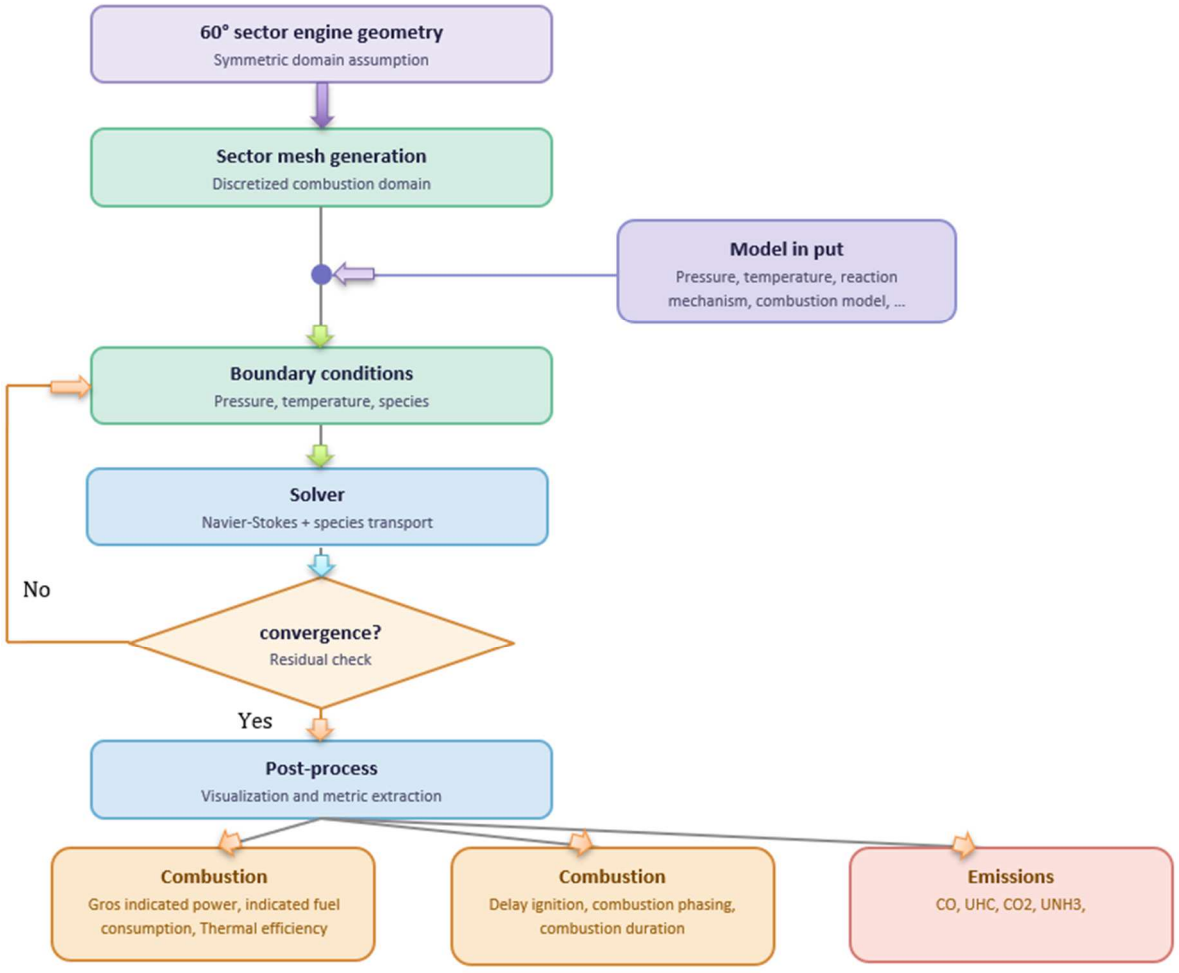

Fig. 1. Overview of computational methodology [45, 46].

Table 1. Engine specifications [17].

Engine model	Characteristics
Number of cylinders	1
Bore and stroke [mm x mm]	137.2 × 165.1
Geometric CR	16.1
Displacement [L]	2.44
Conn. rod length [mm]	261.6
Intake valve close [BTDC]	169.7°
Exhaust valve open [ATDC]	145.3°
Start of injection [BTDC]	14.2°

Table 2. Initial and boundary conditions.

Head temperature (K)	390
Liner temperature (K)	390
Piston temperature (K)	390
Intake pressure (bar)	1.35
Temperature intake (K)	353.15
Inflow droplet temperature (K)	330
Initial swirl ratio	1

Table 3. Spray breakup and collision model parameters [1, 25].

Parameter	Value	Notes
KH Spray Breakup		
KH Size Constant	1.0	Primary atomization control
KH Time Constant	80.0	Breakup timescale (20-80 range)
RT Spray Breakup		
RT Size Constant	1.5	Secondary atomization control
RT Time Constant	1.0	Characteristic time
O'Rourke Secondary		
C_b (Breakup time)	1.0	Breakup time constant
C_σ (Surface tension)	0.5	Surface tension factor
C_τ (Turbulence)	0.4	Turbulence interaction factor

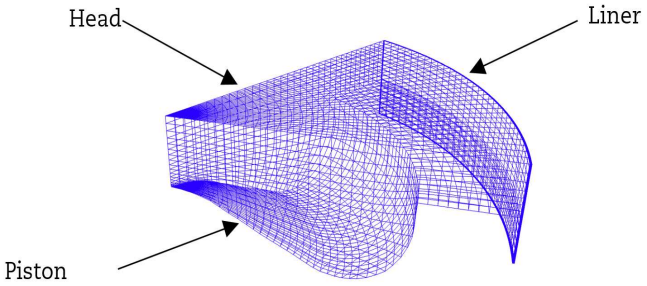

Fig. 2. Computational domain.

3. Computational Domain and Boundary Condition

Ansys Forte was used to perform all simulations. The engine operates at 910 rpm, and computational domain covers the crank-angle interval from intake valve closing (IVC, 169.7° CA BTDC) to exhaust valve closing (EVC, +145.3° ATDC). The analysis focuses on reacting flow dynamics and gas-liquid phase interactions, with emphasis on fuel spray atomization, vaporization, and combustion under varying ASRs. The workflow of numerical study is presented in Fig. 1.

The computational geometry is adopted from Yousefi et al. [17], for model validation. The engine specifications are summarized in Table 1. A piston bowl mesh (60°) is employed, as shown in Fig. 2, to represent the combustion chamber. This choice corresponds to the geometry of a single injector with six periodically arranged nozzle holes. With each nozzle spray covering a 60° sector, the periodicity assumption enables modeling of only one-sixth of the cylinder volume, thereby significantly reducing computational cost. The simulation domain spans the crank angle interval from IVC to EVO. This range captures the full in-cylinder processes of compression, combustion, and expansion. The engine specifications are listed in Table 1.

Swirl motion is initialized with ratio of 1.0 for operation at 910 RPM. The piston bowl geometry and swirl-type intake ports inherently promote rotational air motion, enhancing turbulence at low engine speeds compared with tumble motion [1, 47]. This swirl-driven turbulence improves air-fuel mixing, especially in premixed combustion regimes. The adopted conditions yield turbulence characteristics with velocity fluctuations u' of 2-5 m/s, integral length scales l_I of 1-3 mm, turbulent kinetic energy k ranging from 3-12 m^2/s^2, and dissipation rates ε between 1000-3000 m^2/s^3. These provide realistic and physically consistent initial conditions for the RNG k-epsilon turbulence model, enabling accurate predictions of flame propagation and combustion phasing. Boundary conditions for the cylinder head, liner, and piston surfaces are prescribed as constant wall temperatures (390 K), based on steady-state estimates from experimental single-cylinder engines and prior CFD studies [48]. These temperatures are representative of stabilized single-cylinder operation and were confirmed via ±20 K sensitivity analysis to have negligible impact on combustion phasing and NO_x trends. The parameters are summarized in Table 2.

To ensure a fair energy basis when comparing fuel blends, the ammonia mass fraction in the mixture is adjusted to maintain constant total fuel energy [48]. This is achieved through the ASR, defined as:

$$ASR = \frac{\dot{m}_{\boldsymbol{NH_3}} \times LHV_{\boldsymbol{NH_3}}}{\dot{m}_{\boldsymbol{NH_3}} \times LHV_{\boldsymbol{NH_3}} + \dot{m}_{C_7H_{16}} \times LHV_{C_7H_{16}}} \ (\%) \tag{12}$$

where $\dot{m}_{\boldsymbol{NH_3}}$ and $\dot{m}_{C_7H_{16}}$ are the mass flow rates of ammonia and n-heptane, and $LHV_{\boldsymbol{NH_3}}$ and $LHV_{C_7H_{16}}$ are the respective lower heating values. The KH-RT and O'Rourke collision models are summarized in Table 3.

2.2. Mesh and time step sensitivity

A time step sensitivity analysis (Fig. 3) was performed using 5×10^{-6}, 5×10^{-7} and 5×10^{-8} seconds to evaluate in-cylinder pressure prediction. All cases closely reproduce experimental data, with relative errors below 2.5%. A time step of 5×10^{-7} s provides the optimal balance between accuracy and computational cost and is therefore adopted for all subsequent simulations. A mesh dependency study (Fig. 3(b), Table 4) was conducted with 25,000, 50,000, 100,000 and 200,000 cells, using in-cylinder pressure at Top Dead Center (TDC) as the primary metric. For the 40% ammonia substitution case, the maximum error was approximately 4%, with discrepancies across other cases within 3.5%. The 50,000-cell mesh is selected as the best compromise, capturing small-scale eddies more accurately than coarser grids while avoiding the excessive computational cost of finer meshes. The piston motion was represented using layer addition and removal, ensuring accurate volume changes throughout the engine cycle. In-cylinder pressure is a globally integrated metric sensitive to spray evolution, turbulence, and combustion coupling. Convergence within 3–4% across grids. The final simulation configuration employs a 5×10^{-7} s time step and a 50,000-cell structured hexahedral mesh, providing robust numerical accuracy and efficiency. Structured hexahedral cells reduce numerical diffusion and enhance wall-resolution, which is particularly beneficial for RANS-based simulations.

Table 4. Mesh configuration details for different grid resolutions.

Mesh Case	Total Cell Count	Cell Type	Minimum Cell Size (mm)	Maximum Cell Size (mm)	Growth Rate	Wall Treatment
A	25,000	Hexahedral	0.40	3.50	1.25	Standard wall function
B	50,000	Hexahedral	0.30	3.00	1.15	Standard wall function
C	100,000	Hexahedral	0.20	2.50	1.12	Standard wall function
D	200,000	Hexahedral	0.15	2.00	1.10	Standard wall function

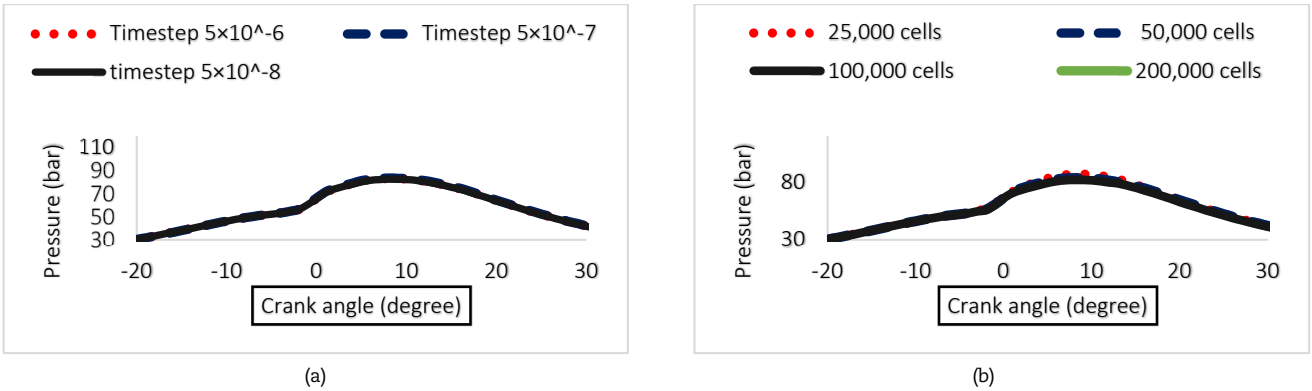

(a) (b)

Fig. 3. Sensitivity, (a) Time step sensitivity, (b) Mesh sensitivity.

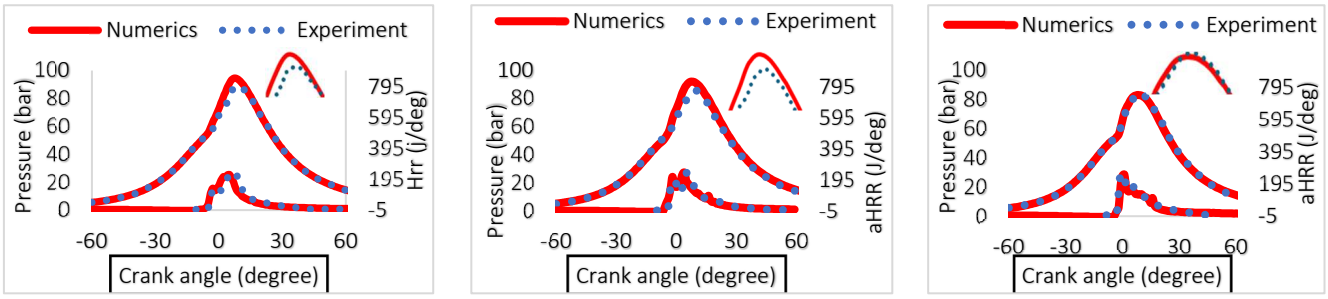

(a) (b) (c)

Fig. 4. In-cylinder pressure and heat release rate, (a) 0% NH_3, (b) 20% NH_3, (c) 40% NH_3.

4. Results and Discussions

This section presents and analyzes the results obtained from the numerical simulations, including comparisons with experimental data for validation purposes [17]. Key parameters such as in-cylinder pressure and heat release rate (HRR) are first evaluated to verify the model's accuracy. Subsequent analyses focus on OH radical concentrations and ammonia mass fractions to better understand ignition and flame development processes. A comprehensive discussion of emissions characteristics–is provided, highlighting the effects of varying ASRs. Furthermore, additional results cover sprays atomization, combustion dynamics and fuel efficiency.

4.1. Model validation

To validate the simulation framework, predicted in-cylinder pressure and apparent heat release rate (HRR) were compared with experimental data for ammonia substitution ratios (ASRs) of 0%, 20%, and 40% (Fig. 4). The numerical results show good agreement with experiments, confirming the predictive capability of the adopted reaction mechanism and turbulence–chemistry models. Increasing ASR reduces peak in-cylinder pressure by up to ~10% at 40% ASR, reflecting ammonia's lower energy density and slower reaction kinetics. HRR curves indicate longer combustion durations with higher ammonia fractions, consistent with ammonia's wider flammability range (15–28%) compared with heptane (1.1–6.7%). At higher ASRs, a secondary HRR peak emerges due to delayed oxidation in stratified ammonia-rich regions, consistent with two-stage RCCI combustion [14, 49].

Figures 4(a) and 4(b) show detailed comparisons for pressure and HRR at 20% and 40% ASR, highlighting extended combustion and the secondary peak. Figure 4 presents RMSE values: 1.8–2.2 bar for pressure and 2.5–3.0 J/°CA for HRR, confirming the quantitative accuracy of the CFD predictions. Notably, the secondary HRR peak visible at 20% ASR (Fig. 4(b)) is absent at 40% ASR (Fig. 4(c)), where instead a single strong and early HRR peak dominates. This behavior is explained by the transition in combustion regime at elevated ASR: at 20% ASR, the ammonia fraction is sufficient to create locally fuel-rich stratified regions that undergo delayed oxidation after the main heptane-driven ignition event, producing the characteristic two-stage heat release. At 40% ASR, the substantially higher ammonia content and associated higher latent heat of vaporization lead to more uniform in-cylinder charge cooling and a more homogeneous mixture prior to ignition. Under these conditions, the heptane pilot ignites the ammonia-air mixture more uniformly and simultaneously across the combustion chamber, resulting in a single sharp and intense HRR peak rather than the sequential two-stage release observed at intermediate ASR. The suppression of the secondary peak at 40% ASR is therefore a consequence of the shift from stratified, sequential oxidation toward more premixed, near-simultaneous combustion driven by the dominant ammonia fraction.

4.2. Spray dynamics

Figure 5 presents a detailed analysis of spray dynamics and vaporization behavior under different ASRs, highlighting their influence on vapor penetration, total vapor mass, droplet size distribution, and wall-film formation within the combustion chamber. Primary and secondary atomization are modeled with the KH-RT, droplet-droplet collisions interaction uses the O'Rourke collision model, wall-film interaction follows a stick/reflect law. Multicomponent evaporation adopts the DMC approach with mixture-average diffusion (NH_3/$C7H_{16}$) and two-way coupling supplies mass, momentum, and scalar source terms to the gas phase [32, 50]. Vaporization is governed by local thermodynamic conditions such as pressure, temperature, turbulence intensity, and species concentration [51, 52]. Combustion is described using a hybrid strategy, where the G-equation resolves premixed flame propagation and is coupled with detailed chemistry model accounting for low-temperature ignition and non-premixed combustion [53]. This adaptive framework ensures that both premixed and diffusion flame regimes are captured simultaneously, depending on local stratification and thermal gradients, which is essential for representing the complex behavior of RCCI combustion.

The vapor penetration length, defined as the axial distance from the nozzle to the point where 99.9% of the injected fuel has vaporized, is shown in Fig. 5(a). At 0% ASR, vapor penetration peak near ~47 mm, while at 20% and 40% ASR it extends to 100 mm and 110 mm, respectively. This extended penetration is a direct consequence of ammonia's high latent heat, which lowers local gas temperatures and delays vapor-phase mixing. Although longer penetration enhances air-fuel mixing, it simultaneously increases the likelihood of piston wall-impingement, which promotes liquid film formation, incomplete combustion, and pollutant emissions. Conversely, too short penetration limits premixing, underlining the importance of balanced vaporization dynamics. The evolution of total vapor mass with crank angle is depicted in Fig. 5(b). At 0% ASR, the maximum vapor mass reaches 0.0118 g, while at 20% ASR it slightly decreases to 0.0115 g. Due to its higher volatility, ammonia vaporizes rapidly and remains in the gaseous phase, particularly in regions of the chamber. Vapor persists from the start of injection at 14.2° BTDC until roughly 18°, during which a significant portion of heptane remains unreacted well to the expansion stroke.

Figure 5(c) illustrates the effect of ammonia substitution ratio (ASR) on the droplet size distribution. The predicted SMD for 0% ASR (pure heptane) is 5.96 µm, indicating effective atomization of the heptane pilot. As ASR increases to 20% and 40%, the SMD rises sharply to 222 µm and 259 µm, respectively. It should be noted that the reported SMD values correspond to the domain-averaged Sauter Mean Diameter over all liquid parcels present in the computational sector at the considered crank angle, including droplets undergoing secondary breakup, coalescence, and wall-interaction processes. The SMD is defined as the ratio of the third to the second moment of the droplet size distribution $(\mathrm{SMD} = \sum \mathrm{di}^3/\mathrm{di}^2)$, thereby weighting droplet according to surface-area-to-volume ratio [54]. As a result, the metric is particularly sensitive to the presence of large coalesced droplets and wall-film fragments. The pronounced increase in SMD at higher ASR therefore reflects the combined effects of reduced spray momentum, enhanced droplet-droplet interaction, and wall impingement, rather than near-nozzle primary atomization alone. When evaluated in a restricted region upstream of wall impingement (near-nozzle zone), the SMD increase is less pronounced, indicating that large domain-averaged values are primarily influenced by downstream coalescence and wall-interaction effects.

Figure 5(d) illustrates the impact of ASR on wall-film. At 0% ASR, no liquid film is detected, indicating complete vaporization before droplets reach the walls. At 20% ASR, a small film with an area of 1.48 cm^2 develops near -0.9 CA, while at 40% ASR, the film area expands substantially to more than 7.4 cm^2 at 1.01 CA. This behavior can be linked both to larger droplet sizes at higher ASRs and to the cooling effect of heptane vaporization, which lowers local in-cylinder temperatures and promotes the persistence of liquid films. Although wall-films can provide localized cooling, their presence disrupts mixture homogeneity, suppresses flame propagation, and leads to higher UHC emissions. Figure 6 illustrates the effect of varying ASR on the in-cylinder temperature evolution during the combustion process. As the ASR increases, peak mean temperature decreases from ~1540 K (0% ASR) to 1500 K (20% ASR), and 1450 K (40% ASR), reflecting lower reactivity and delayed ignition. By CA = +145° ATDC, 20 % ASR sustains higher mean temperatures (~900 K) than 40% ASR (~875 K), indicating reduced heat release at high substitution.

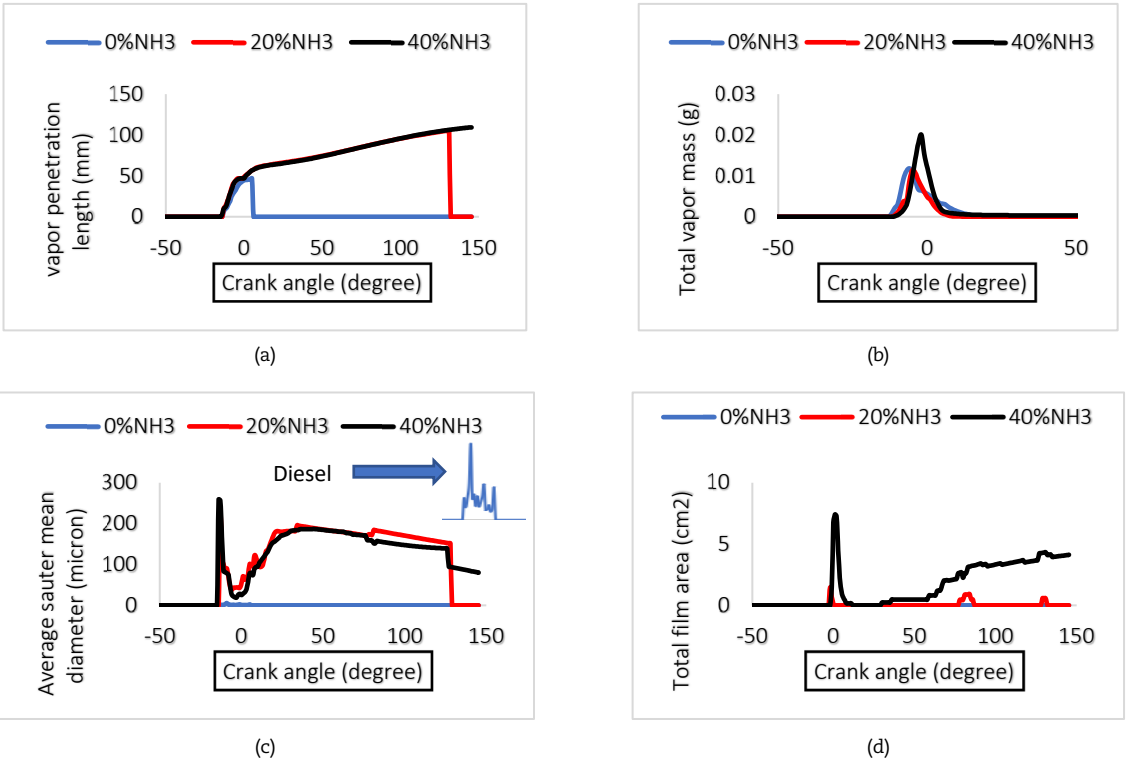

Fig. 5. Spray characteristics, (a) Vapor penetration length, (b) Total vapor mass, (c) Average sauter mean diameter, (d) Total film area.

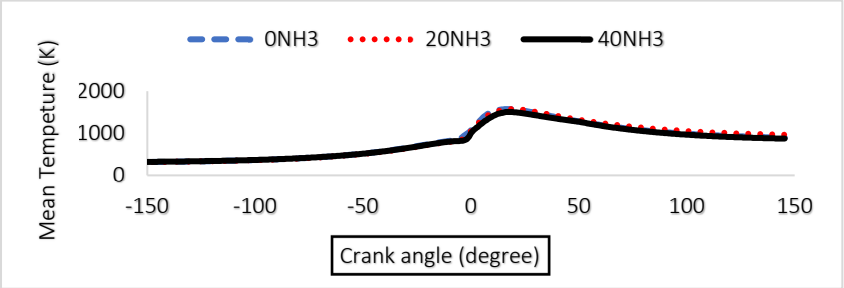

Fig. 6. Effect of varying ammonia substitution on the mean temperature.

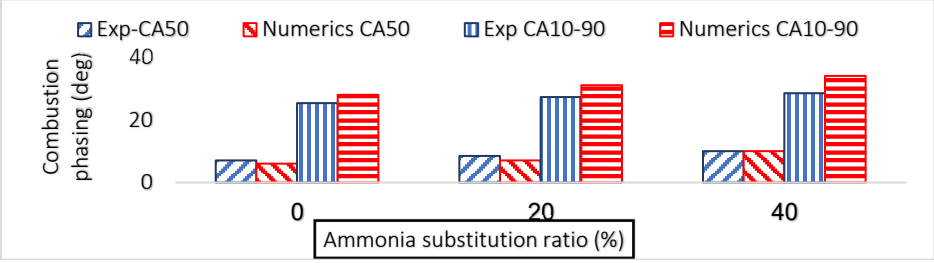

Fig. 7. Influence of ammonia substitution percentages on CA50 and combustion duration (10%-90%).

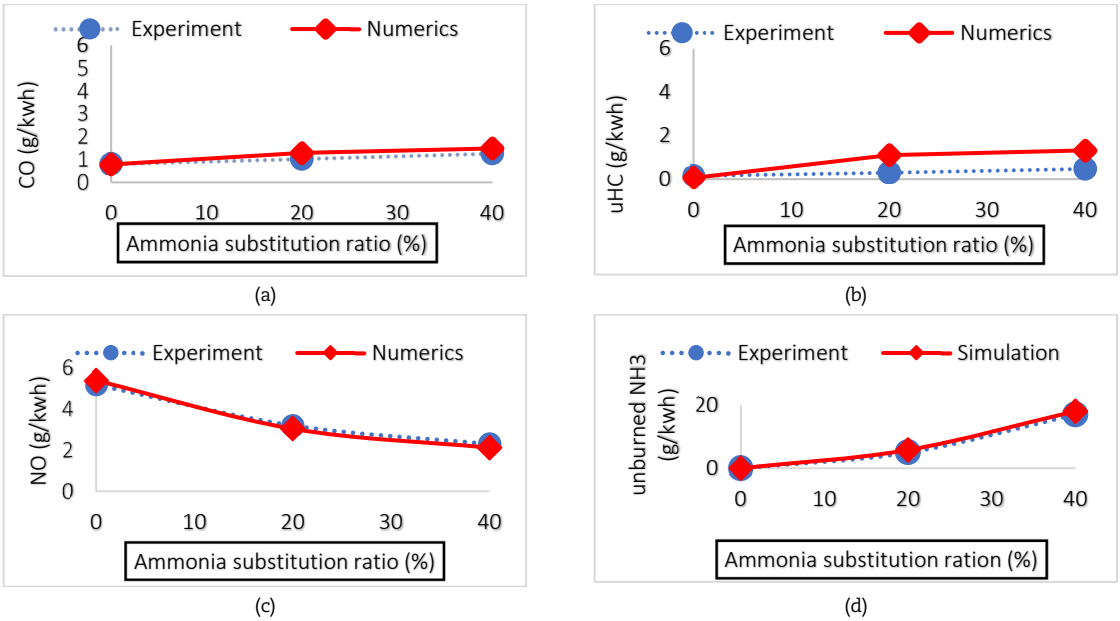

Fig. 8. Comparison of emissions level between experimental data and computational simulations, (a) CO, (b) UHC, (c) NO, and (d) UNH_3.

4.3. Ammonia's impact on combustion

Figure 7 presents combustion phasing (CA10–CA90) for ASRs of 0%, 20%, and 40%. Combustion duration increases from ~24 CAD to ~30 CAD experimentally and from ~28 CAD to ~35 CAD numerically as ASR rises from 0% to 40%, corresponding to an overall increase of ~25–45%. Simulations consistently overpredict burn duration, with the discrepancy growing at higher ASR. This behavior is primarily attributed to slower post-ignition oxidation in ammonia kinetics, RANS-averaged mixing that underrepresents localized ignition acceleration, and simplified wall heat transfer treatment, whose combined effects become more pronounced under ammonia-dominated, temperature-stratified RCCI conditions. At 0% ASR, heptane-dominated combustion yields short durations with good agreement between experiments and simulations. Despite these discrepancies, the simulations capture the correct ASR-dependent phasing trends.

Figure 8 presents the comparison between predicted and experimental emissions of CO, UHC, and NO for ammonia substitution ratios (ASRs) of 0%, 20%, and 40%. Figure 8(a) shows that CO emissions increase with ASR, from ~1.5 g/kWh at 0% ASR to ~5 g/kWh at 40% ASR. The simulations reproduce the overall trend, though CO is overpredicted by 15–20%, likely due to simplified ammonia–heptane chemical kinetics and limitations in turbulence–chemistry coupling that reduce modeled CO oxidation efficiency. Figure 8(b) illustrates that UHC emissions also rise with ASR, particularly in low-temperature or oxygen-deficient regions near walls and crevices. The model overpredicts UHC by ~10–25%, reflecting challenges in resolving local flame quenching, fuel stratification, and incomplete oxidation. Figure 8(c) shows that NO emissions decrease consistently with increasing ASR, from ~3.5 g/kWh at 0% ASR to ~1.7 g/kWh at 40% ASR. Both experiments and simulations closely match this trend, confirming that the model accurately captures thermal NO formation under varying ASR conditions. Figure 8(d) shows that unburned NH_3 emissions increase with ammonia substitution ratio (ASR), from near zero at 0% ASR to ~17–18 g/kWh at 40% ASR. This trend arises from ammonia's lower chemical reactivity, which reduces local combustion temperatures, and from turbulence–chemistry interactions, where incomplete mixing further slows NH_3 oxidation at high ASR. The simulations closely match experiments, confirming that the model accurately captures the coupled effects of ASR, turbulence, and chemical kinetics on ammonia emissions in RCCI operation.

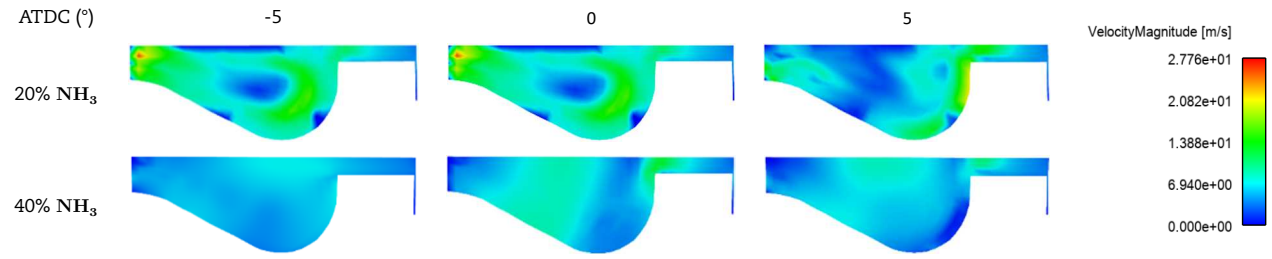

Fig. 9. Velocity magnitude (m/s).

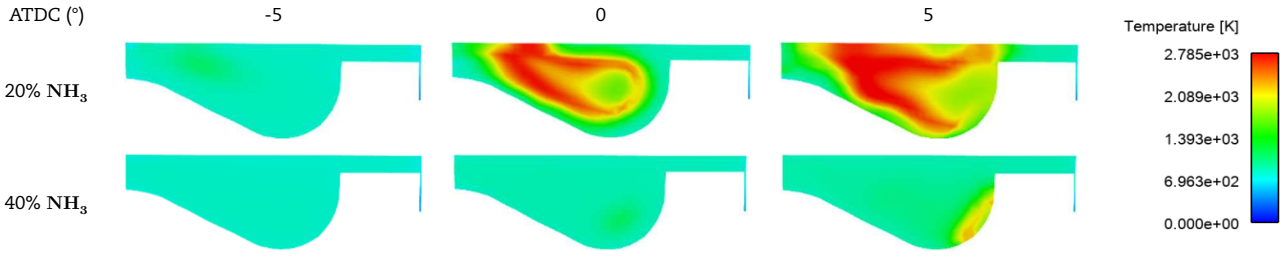

Fig. 10. Temperature distribution.

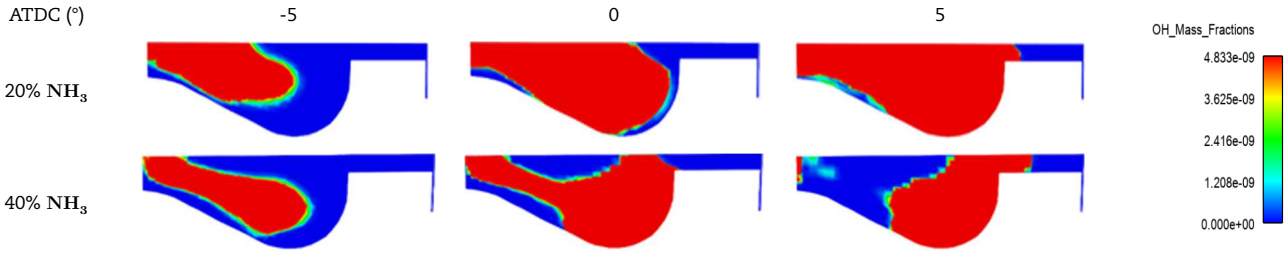

Fig. 11. OH-mass fraction.

4.4. Velocity distribution

Figure 9 presents velocity magnitude contours (m/s) at three representative crank angles, with numerical scales and contour bars included for quantitative assessment. Peak velocities occur near the heptane pilot nozzle due to high injection momentum. As ASR increases, chamber-wide velocities decrease for example, at 20° CA BTDC, volume-averaged velocities drop from ~12 m/s at 0% ASR to ~8 m/s at 40% ASR. This reduction is caused by lower diesel injection mass and momentum at higher ASRs, which shortens spray penetration and weakens turbulence generation. Consequently, fuel–air mixing efficiency is reduced, particularly at later crank angles, where the ammonia-rich charge produces a less energetic flow field. The quantitative velocity fields highlight the influence of ASR on in-cylinder turbulence, mixing, and subsequent combustion behavior.

4.5. Temperature distribution

Figure 10 presents the mean in-cylinder temperature for ASRs of 0%, 20%, and 40%. Increasing ASR reduces peak temperatures due to ammonia's lower reactivity and heating value, which prolongs ignition delay and slows radical-driven chain-branching reactions. At higher ASRs, low-temperature zones appear earlier in the cylinder core, redistributing thermal gradients and potentially reducing local thermal loading. The temperature field also becomes more uniform, reflecting a shift toward more premixed combustion and delayed heat release.

4.6. Hydroxyl radicals (OH)

Figure 11 shows the OH radical mass fraction, a key intermediate reflecting flame front location, radical pool evolution, and local extinction. At 20% ASR, OH concentrations are higher, indicating faster radical pool buildup and more vigorous combustion. At 40% ASR, OH levels decrease sharply, consistent with slower radical formation, delayed ignition, and prolonged combustion duration. The reduced OH intensity and thinner reaction zones at high ASR are consistent with the more premixed, lower-temperature conditions observed in the temperature and flame-structure fields.

4.7. Effects of start of injection

Figure 12 compares the effect of Start of Injection (SOI) on in-cylinder pressure and heat release rate (HRR) at 40% ASR. Figure 12(a) shows that at 14.2° BTDC, late injection limits premixing, resulting in diffusion-dominated combustion with a broad HRR peak and slow pressure rise. Figure 12(b) illustrates that advancing SOI to 16° BTDC increases premixing, producing a sharper HRR peak and steeper pressure rise. Figure 12(c) presents that at 18° BTDC, enhanced premixing shifts combustion closer to TDC, increasing peak pressure and HRR. Figure 12(d) highlights that at 20° BTDC, combustion achieves optimal phasing: a strong premixed spike is followed by controlled diffusion. Simulation and experiment closely align. Figure 12(e) shows that at 22° BTDC, combustion becomes predominantly premixed, initiating earlier and producing a faster pressure rise. Figure 12(f) illustrates that at 24° BTDC, extensive premixing triggers early combustion before TDC, resulting in rapid pressure rise and elevated peak pressure.

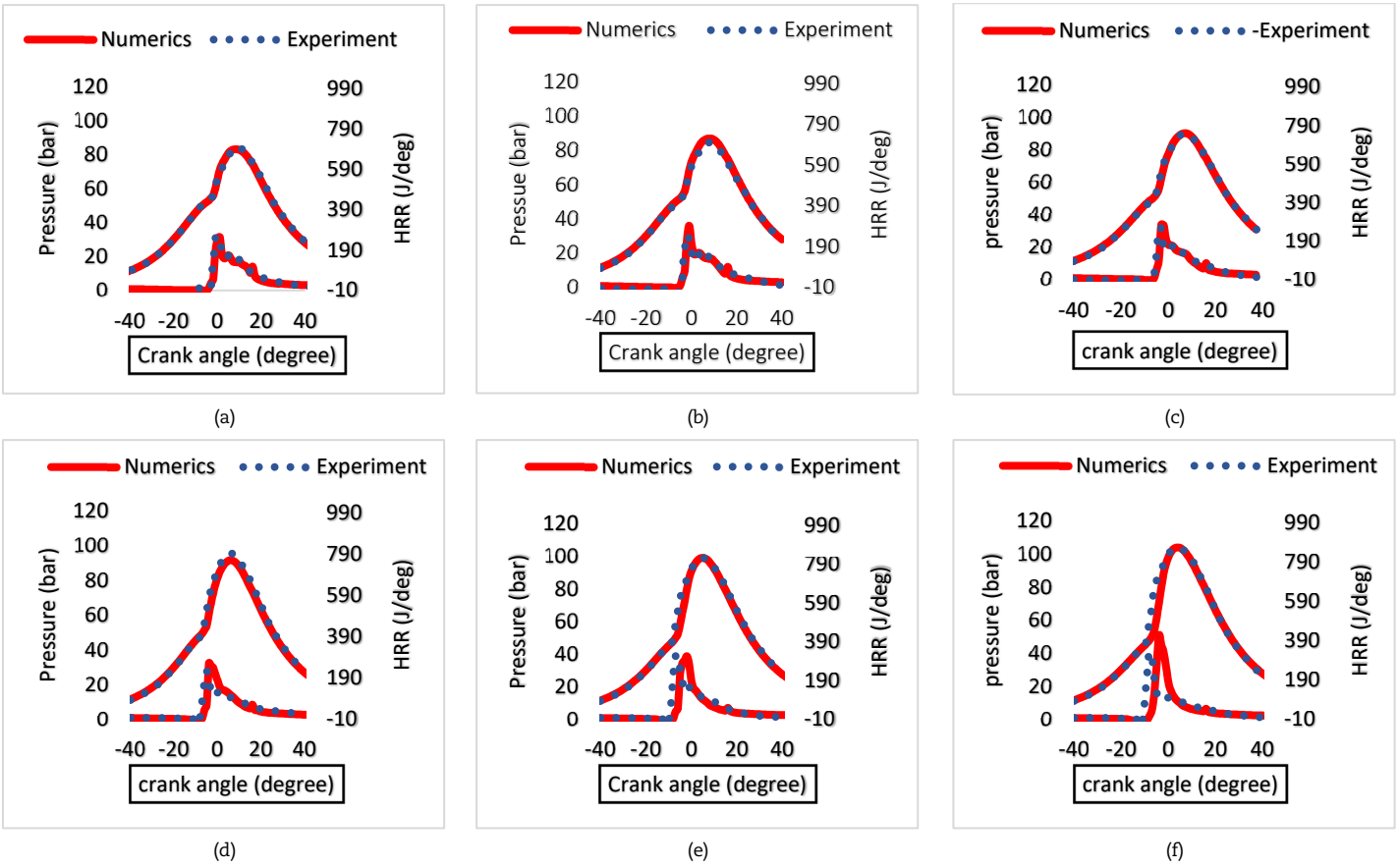

Fig. 12. Effect of start of injection on ammonia 40% concentration, (a) 14.2° BTDC, (b) 16° BTDC, (c) 18° BTDC, (d) 20° BTDC, (e) 22° BTDC, (f) 24° BTDC.

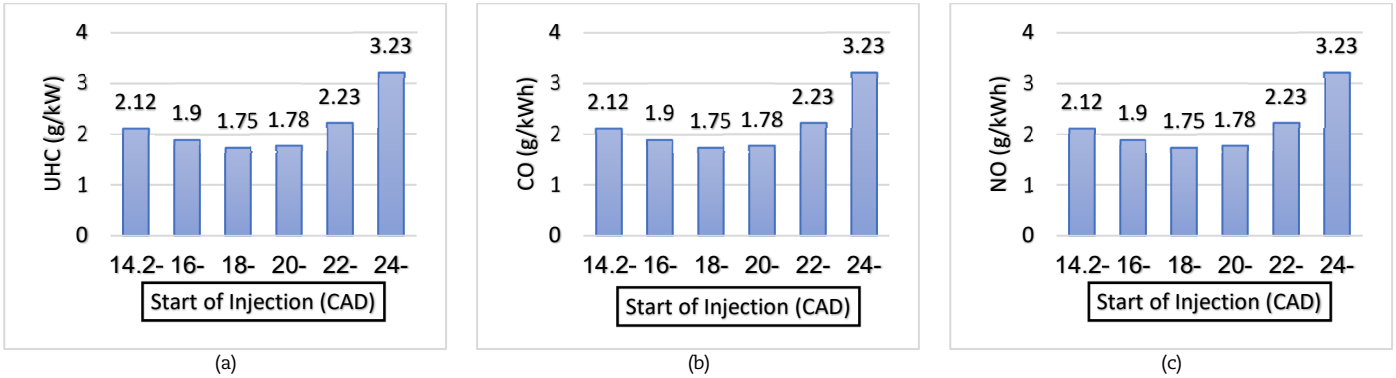

Fig. 13. Impact of SOI on emission, (a) UHC, (b) CO, (c) NO.

4.8. Emissions characteristics under SOI variation

Figure 13 illustrates how SOI influences emissions at 40% ASR. Figure 13(a) shows that UHC emissions peak at 20° BTDC due to limited premixing and shorter ignition delay, leaving more unburned fuel. Advancing SOI to 22°–24° BTDC slightly reduces UHC by improving charge homogenization and post-flame oxidation. Figure 13(b) illustrates that CO emissions increase with advanced SOI, rising from 1.47 g/kWh at 14.2° BTDC to above 5 g/kWh at 22°–24° BTDC. Early combustion lowers in-cylinder temperatures during expansion, reducing CO conversion to CO_2. Figure 13(c) presents that NO emissions remain relatively constant between 14.2° and 20° BTDC but rise sharply at earlier SOIs, reaching 3.23 g/kWh at 24° BTDC, due to higher peak temperatures and longer high-temperature exposure. To move beyond a purely descriptive assessment of injection timing effects, a Pareto-based optimization analysis was conducted to quantify the trade-off between fuel efficiency and emissions at high ammonia substitution. To move beyond qualitative trends, a Pareto-based evaluation was performed to quantify the trade-offs between combustion efficiency and emissions for the SOI sweep at 40% ASR. Figure 14(a) shows the Pareto front between indicated specific fuel consumption (ISFC) and UHC emissions (percent differences relative to the optimal SOI = 16° BTDC). SOI = 16° BTDC provides the best compromise, minimizing both ISFC and UHC. Retarded injection at 14° BTDC slightly increases UHC (+4%) with negligible ISFC change (+0.002%). Advancing SOI beyond 16° increases ISFC (+1.6% at 18° BTDC; +4.9% at 20° BTDC) and UHC (+12–38% at 18–20° BTDC) due to more intense premixed combustion and earlier heat release, reducing overall efficiency. Figure 14(b) presents the Pareto front for ISFC vs NOx emissions (relative to minimum NO_x of 1.75 g/kWh at 18° BTDC). Advancing SOI initially reduces NO_x (–1.3% at 16° BTDC), but SOI beyond 20° BTDC sharply increases NOx (+85% at 24° BTDC) while slightly increasing ISFC (+0.3–4.9%). Retarded injections (14–16° BTDC) maintain lower ISFC but moderately higher NOx (+8–21%). The Pareto-optimal range lies between 16°–18° BTDC, providing the best trade-off between fuel efficiency and emissions. SOI = 20° BTDC, though favorable for combustion stability, is sub-optimal in the efficiency–emission balance.

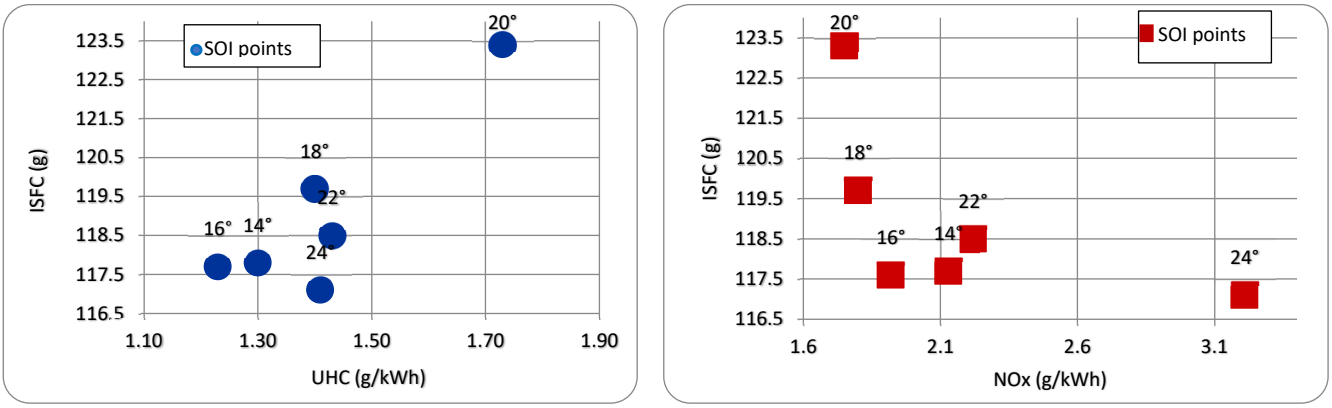

(a) (b)

Fig. 14. Pareto analysis of ammonia RCCI combustion showing the trade-off between fuel efficiency and emissions for varying SOI timings, (a) ISFC vs UHC (% difference relative to SOI = 16° BTDC), (b) ISFC vs NO_x.

5. Conclusion

This study investigated ammonia substitution in a heptane-fueled RCCI engine using a validated high-fidelity framework with detailed chemistry, hybrid G-equation combustion, and RANS turbulence. Increasing ammonia (ASR 0–40%) reduces peak pressure and heat release (~3–4%), prolongs combustion, shifts phasing, and increases vapor penetration and wall-film formation, affecting CO and UHC emissions. Injection timing strongly influences emissions: UHC peaks at 1.73 g/kWh for retarded SOI (20° BTDC) and declines slightly at advanced SOI (22–24° BTDC), CO rises from 1.47 g/kWh at 14.2° BTDC to over 5 g/kWh at 22–24° BTDC, and NO remains nearly constant up to 20° BTDC but reaches 3.23 g/kWh at 24° BTDC. Pareto analysis at 40% ASR identifies SOI = 16° BTDC as optimal for efficiency and UHC, with 16–18° BTDC providing a compromise for NO_x control. ASR should not exceed 40% for stable ignition under these conditions, emphasizing the importance of SOI optimization for low-carbon RCCI engine design. Future work will extend to LES, multi-cylinder configurations, and aftertreatment integration.

Author Contributions

The authors have confirmed their contributions to this study as follows: S. Molima was responsible for formal analysis and drafting the original manuscript; F. Hamdi and T. Hamdi contributed to formal analysis and editing the original draft; and M. Chrigui oversaw conceptualization and supervision. The manuscript was written through the contribution of all authors. All authors discussed the results, reviewed, and approved the final version of the manuscript.

Acknowledgments

Not applicable.

Conflict of Interest

The authors declared no potential conflicts of interest concerning the research, authorship, and publication of this article.

Funding

The authors received no financial support for the research, authorship, and publication of this article.

Data Availability Statements

Not applicable.

Nomenclature

CA10-90	Combustion duration	ICE	Internal combustion engine
CA50	50% of total fuel energy released during the combustion	ICEs	Internal combustion engines
ASR(s)	Ammonia substitution ratio(s)	ITE	Indicated thermal efficiency
ATDC	After top dead center	IVC	Intake valve close
BTDC	Before top dead center	LHV	Lower heating value
CFD	Computational fluid dynamics	LNG	Liquefied natural gas
CI	Compression ignition	NO	Nitric oxide
CO	Carbon monoxide	NOx	Nitrogen oxides
CO2	Carbon dioxide	OH	Hydroxyl radicals
CR	Compression ratio	PM	Particulate matter
DI	Direct injection	RCCI	Reactivity controlled-compression ignition
DOI	Duration of Injection	RNG	Renormalization Group
DMC	Discrete Multi Component	SMD	Sauter mean diameter
EVO	Exhaust valve open	SOI	Start of Injection
GHG	Greenhouse gas	TDC	Top dead center

HC	Hydrocarbon	THC	Total hydrocarbon
HRR	Heat release rate	TKE	Turbulence kinetic energy, $\mathrm{m}^2.\mathrm{s}^{-2}$

Symbols

D	Diffusion coefficient of species	S_L^O	Laminar flame speed
$\bar{F}^s$	Source term due to spray injection	S_T^O	Turbulent flame speed
Γ	Stress tensor that accounts for the effects of ensemble averaging	$\vec{u}$	Velocity vector
$\Gamma_{\Phi,T}$	Turbulent exchange coefficient of Φ	$\tilde{u}$	Favre averaged velocity
H	Heat flux	u'	Turbulence intensity
$\tilde{h}_k$	Specific enthalpy of species	$\nabla\bar{T}$	Gradient of temperature field in the fluid
$\vec{J}$	Diffusion flux	$\tilde{\varepsilon}$	Dissipation rate
$\tilde{K}$	Favre mean flame front curvature	$\nabla\bar{y}_k$	Gradient of the concentration of species k'
$\tilde{k}$	Favre mean turbulent kinetic energy	$\dot{\tilde{W}}^S$	Quantity accounts for the contribution due to evaporating droplets
λ	Thermal conductivity	$\overline{\rho}$	Fluid density
l_F	Laminar flame thickness	$\bar{\rho}_u$	Densities of burned mixture
l_I	Turbulence Integral length scale	$\bar{\rho}_b$	Densities of fresh
$\dot{m}_{\boldsymbol{n-heptane}}$	Heptane mass flow rate	$\dot{\bar{\rho}}_m^S$	Source term due to sprays' vaporization
$\dot{m}_{\boldsymbol{NH_3}}$	Ammonia mass flow rate	$\dot{\bar{\rho}}_m^C$	Source term due to chemical reactions
q_i	Rate of progress of specified reaction i	$\dot{\omega}_{mi}$	Production dissipation rate of the mth species in the ith reaction
$\dot{\tilde{Q}}^C$	Source terms due to heat released	$\bar{\sigma}$	Averaged viscous shear stress tensor
$\dot{\tilde{Q}}^S$	Source terms due to spray interaction		

References

[1] Molima, S., Hamdi, F., Hamdi, T., Muya, G. T., Mondo, K., Amsini, S., Chrigui, M., Effects of H2 substitution on combustion and emissions in ammonia/diesel compression ignition engine, *Energy Conversion and Management*, 334, 2025, 119858.

[2] Cheng, Q., Muhammad, A., Kaario, O., Ahmad, Z., Martti, L., Ammonia as a sustainable fuel: Review and novel strategies, *Renewable and Sustainable Energy Reviews*, 207, 2025, 114995.

[3] Shin, W., Lai, H., Ibrahim, G., Zang, G., Toward a sustainable energy future using ammonia as an energy carrier: global supply chain cost and greenhouse gas emissions, *Energy & Environmental Science*, 19(1), 2026, 162–188.

[4] Cornelius, W., Huellmantel, L.W., Mitchell, H.R., Ammonia as an engine fuel, *SAE Transactions*, 650052, 1966, 300–326.

[5] Garabedian, C.G., Johnson, J.H., The theory of operation of an ammonia burning internal combustion engine, *Army Tank-Automotive Center*, 1966, 333–348.

[6] Starkman, E.S., Newhall, H., Sutton, R., Maguire, T., Farbar, L., Ammonia as a spark ignition engine fuel: theory and application, *SAE Transactions*, 1967, 765–784.

[7] Pearsall, T.J., Garabedian, C.G., Combustion of anhydrous ammonia in diesel engines, *SAE Transactions*, 1968, 3213–3221.

[8] Mounaïm-Rousselle, C., Brequigny, P., Ammonia as fuel for low-carbon spark-ignition engines of tomorrow's passenger cars, *Frontiers in Mechanical Engineering*, 6, 2020, 70.

[9] Grannell, S.M., Assanis, D.N., Bohac, S.V., Gillespie, D.E., The fuel mix limits and efficiency of a stoichiometric, ammonia, and gasoline dual fueled spark ignition engine, *Journal of Engineering for Gas Turbines and Power*, 130, 2008, 042802.

[10] Wang, B., Wang, H., Hu, D., Yang, C., Duan, B., Wang, Y., Effect of different ammonia mixing methods for diesel ignition on combustion and emission performance of high pressure common rail engine, *Journal of the Energy Institute*, 111, 2023, 101402.

[11] Liu, J., Liu, J., Experimental investigation of the effect of ammonia substitution ratio on an ammonia-diesel dual-fuel engine performance, *Journal of Cleaner Production*, 434, 2024, 140274.

[12] Reiter, A.J., Kong, S.-C., Combustion and emissions characteristics of compression-ignition engine using dual ammonia-diesel fuel, *Fuel*, 90(1), 2011, 87–97.

[13] Tay, K. L., Yang, W., Chou, S. K., Zhou, D., Li, J., Yu, W., ..., & Mohan, B., Effects of injection timing and pilot fuel on the combustion of a kerosene-diesel/ammonia dual fuel engine: a numerical study, *Energy Procedia*, 105, 2017, 4621–4626.

[14] Nadimi, E., Przybyła, G., Lewandowski, M.T., Adamczyk, W., Effects of ammonia on combustion, emissions, and performance of the ammonia/diesel dual-fuel compression ignition engine, *Journal of the Energy Institute*, 107, 2023, 101158.

[15] Xu, L., Xu, S., Bai, X.-S., Repo, J.A., Hautala, S., Hyvönen, J., Performance and emission characteristics of an ammonia/diesel dual-fuel marine engine, *Renewable and Sustainable Energy Reviews*, 185, 2023, 113631.

[16] Shin, J., Park, S., Numerical analysis and optimization of combustion and emissions in an ammonia-diesel dual-fuel engine using an ammonia direct injection strategy, *Energy*, 289, 2024, 130014.

[17] Yousefi, A., Guo, H., Dev, S., Liko, B., Lafrance, S., Effects of ammonia energy fraction and diesel injection timing on combustion and emissions of an ammonia/diesel dual-fuel engine, *Fuel*, 314, 2022, 122723.

[18] Bjørgen, K.O.P., Emberson, D.R., Løvås, T., Combustion of liquid ammonia and diesel in a compression ignition engine operated in high-pressure dual fuel mode, *Fuel*, 360, 2024, 130269.

[19] Elkelawy, M., Bastawissi, H.A.-E., Elsamadony, M.O., Abdalhadi, A.S., Engine performance and emissions improvement study on direct injection of diesel/ammonia dual fuel by adding CNG as partially premixed charge, *Journal of Engineering Research*, 7, 2024, 12.

[20] Tutak, W., Jamrozik, A., Grab-Rogaliński, K., Pyrc, M., Effects of ammonia energy fraction on combustion stability and emissions characteristics of naturally aspired industrial dual-fuel diesel engine, *Energy Conversion and Management*, 314, 2024, 118698.

[21] Shi, C., Zhang, Z., Wang, H., Wang, J., Cheng, T., Zhang, L., Parametric analysis and optimization of the combustion process and pollutant performance for ammonia-diesel dual-fuel engines, *Energy*, 296, 2024, 131171.

[22] Cheng, C., Cordtz, R.F., Førby, N.L., Schramm, J., Experimental and simulation investigation of n-heptane/ammonia dual fuel on a light-duty compression ignition engine, *International Journal of Hydrogen Energy*, 57, 2024, 1339–1353.

[23] Mi, S., et al., Potential of ammonia energy fraction and diesel pilot-injection strategy on improving combustion and emission performance in an ammonia-diesel dual fuel engine, *Fuel*, 343, 2023, 127889.

[24] Echekki, T., Mastorakos, E., Turbulent combustion: concepts, governing equations and modeling strategies, *Turbulent Combustion Modeling: Advances, New Trends and Perspectives*, 2011, 19–39.

[25] Hamdi, T., Hamdi, F., Molima, S., Hernandez, J.J., Chrigui, M., Computational analysis on the effect of methanol energy ratio on the spray and combustion pattern of a dual-fuel compression ignition engine, *Journal of Energy Resources Technology Part A: Sustainable and Renewable Energy*, 1(4), 2025, 042303.

[26] Cameretti, M.C., De Robbio, R., Palomba, M., Zucareli de Souza, T., Strategies to improve ammonia combustion in a dual fuel marine engine by using CFD, *Fuel*, 381, 2025, 133440.
[27] Han, Z., Reitz, R.D., Turbulence modeling of internal combustion engines using RNG κ-ε models, *Combustion Science and Technology*, 106(4–6), 1995, 267–295.
[28] Sadiki, A., Agrebi, S., Ries, F., Entropy generation analysis in turbulent reacting flows and near wall: a review, *Entropy*, 24(8), 2022, 1099.
[29] Kolhe, A.V., Shelke, R.E., Khandare, S.S., Combustion modeling with CFD in direct injection CI engine fuelled with biodiesel, *Jordan Journal of Mechanical & Industrial Engineering*, 9(1), 2015.
[30] Bayramoglu, K., Yılmaz, S., Emission and performance estimation in hydrogen injection strategies on diesel engines, *International Journal of Hydrogen Energy*, 46(57), 2021, 29732–29744.
[31] Samimi Abianeh, O., Chen, C.P., A discrete multicomponent fuel evaporation model with liquid turbulence effects, *International Journal of Heat and Mass Transfer*, 55(23), 2012, 6897–6907.
[32] Beale, J.C., Reitz, R.D., Modeling spray atomization with the Kelvin-Helmholtz/Rayleigh-Taylor hybrid model, *Atomization and Sprays*, 9(6), 1999.
[33] Lewandowski, M.T., Netzer, C., Emberson, D.R., Løvås, T., Numerical investigation of optimal flow conditions in an optically accessed compression ignition engine, *Transportation Engineering*, 2, 2020, 100036.
[34] Selvaraj, P., et al., A computational study of ethylene–air sooting flames: effects of large polycyclic aromatic hydrocarbons, *Combustion and Flame*, 163, 2016, 427–436.
[35] Hidouri, A., Yahya, N., Boushaki, T., Sadiki, A., Sautet, J.C., Numerical and experimental investigation of turbulent three separated jets, *Applied Thermal Engineering*, 104, 2016, 153–161.
[36] Mondo, K., Agrebi, S., Hamdi, F., Lakhal, F., Sadiki, A., Chrigui, M., Impact of multi-component surrogates on the performances, pollutants, and exergy of IC engines, *Entropy*, 24(5), 2022, 671.
[37] Chrigui, M., Masri, A., Sadiki, A., Janicka, J., Large eddy simulation of a polydisperse ethanol spray flame, *Flow Turbulence and Combustion*, 90, 2013, 813–832.
[38] Tan, Z., Reitz, R.D., An ignition and combustion model based on the level-set method for spark ignition engine multidimensional modeling, *Combustion and Flame*, 145(1), 2006, 1–15.
[39] Liang, L., Reitz, R.D., Spark ignition engine combustion modeling using a level set method with detailed chemistry, *SAE Technical Paper*, 2006, No. 2006-01-0243.
[40] Yoshikawa, T., Reitz, R.D., Validation of a grid independent spray model and fuel chemistry mechanism for low temperature diesel combustion, *International Journal of Spray and Combustion Dynamics*, 1(3), 2009, 283–316.
[41] Singh, S., Reitz, R.D., Musculus, M.P., Comparison of combustion models against optical diagnostic data for multi-mode combustion in a heavy-duty DI diesel engine, *SAE Transactions*, 2006, 61–82.
[42] Xu, C., Zhong, A., Wang, C., Jiang, C., Li, X., Zhou, K., Huang, Y., Combustion characteristics and laminar flame speed of premixed ethanol-air mixtures with laser-induced spark ignition, *Biofuels Engineering*, 2(1), 2017, 63–72.
[43] Rakopoulos, C.D., Giakoumis, E.G., Second-law analyses applied to internal combustion engines operation, *Progress in Energy and Combustion Science*, 32(1), 2006, 2–47.
[44] Wang, B., Dong, S., Jiang, Z., Gao, W., Wang, Z., Li, J., ..., Cheng, X., Development of a reduced chemical mechanism for ammonia/n-heptane blends, *Fuel*, 338, 2023, 127358.
[45] Molima, S., Hamdi, F., Hamdi, T., Chrigui, M., Multiphase combustion modeling of ammonia–diesel RCCI engines using RANS, DES, and LES turbulence models, *International Journal of Engine Research*, 2026, DOI: 10.1177/14680874261418173.
[46] Hamdi, T., Hamdi, F., Molima, S., Domínguez, V. M., Rodríguez-Fernández, J., Hernández, J. J., Chrigui, M., Numerical investigation of hydrogen substitution ratio effects on spray characteristics, combustion behavior, and emissions in a dual-fuel compression ignition engine, *Machines*, 13(10), 2025, 880.
[47] Bari, S., Saad, I., CFD modelling of the effect of guide vane swirl and tumble device to generate better in-cylinder air flow in a CI engine fuelled by biodiesel, *Computers & Fluids*, 84, 2013, 262–269.
[48] Hamdi, F., Molima, S., Hamdi, T., Chrigui, M., Eulerian–Lagrangian study of the effects of piston geometry on liquid spray and combustion of ammonia–diesel dual-fuel engine, *Applied Thermal Engineering*, 285, 2025, 129284.
[49] Shin, J., Park, S., Numerical analysis for optimizing combustion strategy in an ammonia-diesel dual-fuel engine, *Energy Conversion and Management*, 284, 2023, 116980.
[50] Zhang, Y., Bian, Y., Zhang, Z., Liu, Z., Jia, M., Development of a universal constant set in the Kelvin-Helmholtz Rayleigh-Taylor (KH-RT) breakup model for spray simulations of various fuels, *Atomization and Sprays*, 34(10), 2024, 29-55.
[51] Šikalo, Š., Ganic, E., Phenomena of droplet–surface interactions, *Experimental Thermal and Fluid Science*, 31(2), 2006, 97–110.
[52] Yarin, A.L., Drop impact dynamics: splashing, spreading, receding, bouncing, *Annual Review of Fluid Mechanics*, 38(1), 2006, 159–192.
[53] Schneider, E., Sadiki, A., Janicka, J., Modeling and 3D-simulation of the kinetic effects in the post-flame region of turbulent premixed flames based on the G-equation approach, *Flow Turbulence and Combustion*, 75(1), 2005, 191–216.
[54] Pacek, A.W., Man, C.C., Nienow, A.W., On the Sauter mean diameter and size distributions in turbulent liquid/liquid dispersions in a stirred vessel, *Chemical Engineering Science*, 53(11), 1998, 2005–2011.

ORCID iD

Samuel Molima https://orcid.org/0009-0006-1901-878X
Fathi Hamdi https://orcid.org/0000-0003-1404-1973
Takwa Hamdi https://orcid.org/0009-0003-6974-4446
Mouldi Chrigui https://orcid.org/0000-0002-2775-6436

How to cite this article: Molima S., Hamdi F., Hamdi T., Chrigui M. Modeling of the Ammonia Substitution Ratio in a Heptane-Fueled Internal Combustion Engine, *J. Appl. Comput. Mech.*, xx(x), 2026, 1–13. https://doi.org/10.22055/jacm.2026.48727.5456